



Time-dependent variations in vertical fluxes of hydrothermal plumes at mid-ocean ridges

Xubo Zhang^{1,2,3} · Jian Lin^{2,1,4}  · Houshuo Jiang³

Received: 3 April 2018 / Accepted: 16 July 2018
© Springer Nature B.V. 2018

Abstract

We investigated the short-period variations in vertical fluxes of hydrothermal plumes at mid-ocean ridges through quantitative analysis of digital video images of plumes using the particle image velocimetry method. The analyzed digital video images of hydrothermal plumes were selected from the V Vent and Biotransect Vent at the fast-spreading East Pacific Rise, the Grotto Mound of the Endeavour Segment at the intermediate fast-spreading Juan de Fuca Ridge, and the TAG vent at the slow-spreading Northern Mid-Atlantic Ridge. The PIV was able to track the motion of turbulent parcels instead of individual particles within a hydrothermal plume. The mean plume vertical flux was shown to increase with increasing height above the vent orifice, revealing significant turbulent disperse of the rising hydrothermal plumes. The dominant periods of oscillation in the mean vertical flux were observed to be within a relatively narrow band width of 0.5–5 s despite diverse geological settings. Such pervasive short-period variations in plume flux are hypothesized to be caused by the pressure-drop oscillation within a network of compressible two-phase fluid within a sub-seafloor hydrothermal source zone. It is further argued that both the period and amplitude of plume flux oscillation might increase with decreasing plume vertical flux. The relatively narrow band width of the observed oscillation periods might reflect common characteristics in the plume dynamics despite diverse geological settings.

Keywords Mid-ocean ridge · Hydrothermal plume · Vertical flux · Entrainment coefficient · Short-period oscillation · Pressure-drop oscillation

Electronic supplementary material The online version of this article (<https://doi.org/10.1007/s11001-018-9364-5>) contains supplementary material, which is available to authorized users.

✉ Jian Lin
jlin@whoi.edu

- ¹ State Key Laboratory of Marine Geology, School of Ocean and Earth Science, Tongji University, Shanghai 200092, China
- ² Department of Geology and Geophysics, Woods Hole Oceanographic Institution, Woods Hole, MA 02543, USA
- ³ Department of Applied Ocean Physics and Engineering, Woods Hole Oceanographic Institution, Woods Hole, MA 02543, USA
- ⁴ Key Laboratory of Ocean and Marginal Sea Geology, South China Sea Institute of Oceanology, Chinese Academy of Sciences, Guangzhou 510301, China

Introduction

Seafloor hydrothermal systems play a key role in the transfer of heat and chemicals from the Earth's lithosphere to the oceans (Kadko 1993; Elderfield and Schultz 1996; Baker 2007). It was proposed that as much as 34% of the Earth's global heat flux might be transferred through the seafloor via hydrothermal venting (Stein and Stein 1994; Elderfield and Schultz 1996; German and Von Damm 2006). However, hydrothermal vents show dramatic variability at regional and local scales; thus, it is important to quantify the fluxes of hydrothermal plumes at individual vents.

Two main methods have been employed to estimate hydrothermal plume velocities and vertical fluxes. In the first method, i.e., the invasive method, devices are used to directly measure plume velocities but the physical contact of a device with the plume might interfere with the venting processes. For example, turbine flow meters were deployed at the hydrothermal vents at the East Pacific Rise (EPR) and the Juan de Fuca Ridge (JdFR) to estimate plume

flow velocities (Converse et al. 1984; Ginster et al. 1994; Germanovich et al. 2015). In the second method, i.e., the non-invasive method, devices have no physical contact with the plume and thus do not interfere with the venting processes; as a result, this method has been widely used. For example, the acoustic Doppler velocimetry (ADV) was used to measure plume velocities and fluxes (Jackson et al. 2003; Xu and Di Iorio 2012; Xu et al. 2013, 2014). Moreover, video image frames were analyzed to investigate tidal oscillations of hydrothermal plumes (Corliss et al. 1979; Macdonald et al. 1980; Rona and Trivett 1992; Ramondenc et al. 2006; Crone et al. 2008, 2010; Mittelstaedt et al. 2010, 2012, 2016; Escartín et al. 2013).

Over the past decades, a large number of studies have observed significant variations in flow rates, venting temperatures, chemical compositions, bottom pressures, and microseismicities at different hydrothermal systems over a broad range of time scales, ranging from a few days to a few months, and even up to years (e.g., Little et al. 1988; Schultz et al. 1996; Tivey et al. 2002; Scheirer et al. 2006; Larson et al. 2007, 2009; Crone et al. 2010; Xu et al. 2013, 2017; Barreyre et al. 2014; Mittelstaedt et al. 2016). For example, it was hypothesized that the observed tidal oscillations in a hydrothermal system were caused either by the tide-driven bottom currents (Little et al. 1988; Tivey et al. 2002) or by the poroelastic response of crustal fluids to seafloor tidal loading (e.g., Larson et al. 2007, 2009; Barreyre et al. 2014; Barreyre and Sohn 2016; Xu et al. 2017). The bottom pressure at the TAG hydrothermal field on the Mid-Atlantic Ridge (MAR) at 26°N was measured to vary at periods of 22–53.2 min, indicating a nonlinear relationship between the pore fluid pressure and crustal permeability (Sohn et al. 2009). However, measurements using the same technique did not detect similar short-period signals at the EPR 9°50' (Carbotte et al. 2004). In contrast, Sohn et al. (1995) observed microseismicity with distinct periods of 0.07–0.3 s at the southern Juan de Fuca Ridge (JdFR) and postulated that this microseismicity was caused by transient pressure and hydraulic fracturing within the hydrothermal system. Black smoker hydrothermal vents could produce numerous narrowband tones at periods ranging 0.004–0.1 s (Crone et al. 2006). However, plume oscillations at period range of a few seconds have rarely been investigated.

In this study, we applied a non-invasive measurement technique—the particle image velocimetry (PIV)—to analyze videos of hydrothermal plumes at multiple mid-ocean ridge settings. We first analyzed the plume velocity fields and near steady-state features and then quantified the temporal variations in vertical fluxes of plumes. The results revealed the predominant, significant temporal variations at periods of 0.5–5 s at all studied vents. The pressure-drop oscillations in seafloor hydrothermal systems were proposed

to explain the observed short-period oscillations in plume vertical fluxes.

Data

Digital videos of hydrothermal plumes were selected at the fast-spreading East Pacific Rise (EPR), the intermediate-spreading Juan de Fuca Ridge (JdFR), and the slow-spreading Northern Mid-Atlantic Ridge (NMAR) (Fig. 1a). These digital videos were archived at the Data Library and Archives of the Woods Hole Oceanographic Institution (WHOI). At the EPR (Fig. 1b), videos of the plumes at the V Vent (Fig. 2a) were recorded during the *Alvin Dive 3760* in 2002. The average spatial scale is 2.06 mm/pixel, which was estimated using the reference length scale of the submersible temperature probe. Videos of the plumes at the Biotransect Vent (Fig. 2b) were recorded during the *Alvin Dive 3769* in 2002. At the JdFR (Fig. 1c), the video of the hydrothermal plume at the Grotto mound of the Endeavour Segment (Fig. 2c) was recorded by ROV *Jason* in 2015; the video was obtained online at the Ocean Networks Canada (<http://www.oceannetworks.ca>). The average spatial scale is 0.52 mm/pixel, which was estimated using the 10 cm-spacing laser dots hitting on the plume. At the NMAR (Fig. 1d), two videos of the hydrothermal plumes at the TAG Vent were selected: One video was recorded during the *Alvin Dive 3895* in 2003, in which two plumes were clearly observed (Fig. 2d). The other video was recorded at an unknown date (Fig. 2e). In this study, the plume at the V Vent was marked as Plume A (Fig. 2a), the plume at the Biotransect Vent was marked as Plume B (Fig. 2b), the plume at the Grotto mound of the Endeavour Segment was marked as Plume C (Fig. 2c), and the three individual plumes at the TAG Vent were marked as Plumes D, E (Fig. 2d) and F (Fig. 2e), respectively.

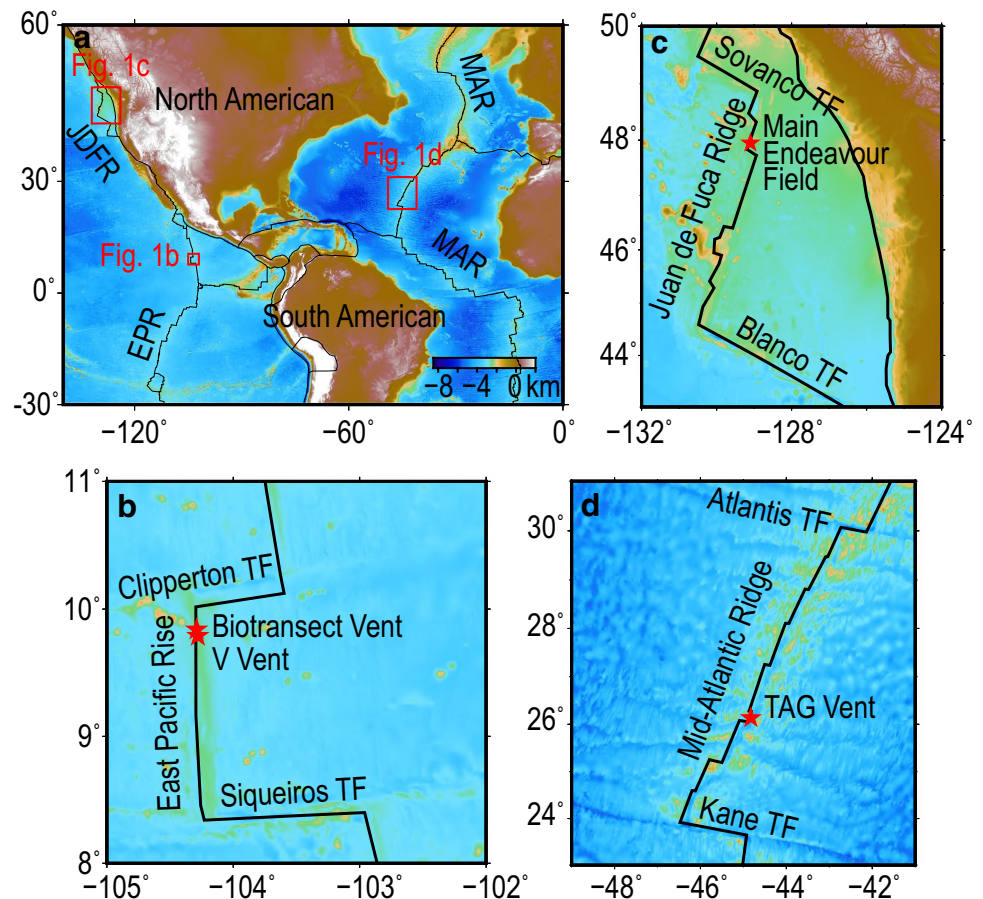
All the video clips were transferred to digital data, archiving at a frame rate of 1/29.97 s between consecutive frames. Each video clip was selected to cover a recorded duration of 10–20 s, during which the submersible vehicle that took the video remained mostly immobile. In each video, the vent orifice was clearly visible, with the plume spanning approximately 500–1000 pixels above the orifice (Fig. 2).

Methods

Image processing

The image processing of each video clip consisted of three steps. First, each video clip was decomposed into a series of still color RGB image frames. In this step, the digital video clips were read by the Matlab function *VideoReader*, which

Fig. 1 **a** Location map of the study areas. **b** Detailed map for a section of the fast-spreading East Pacific Rise (EPR). The red stars mark the locations of the V Vent and the Biotranssect Vent. **c** Detailed map of the Juan de Fuca Ridge (JdFR), which has an intermediate-spreading rate. The red star marks the location of the Main Endeavour Field. **d** Detailed map of a section of the slow-spreading Northern Mid-Atlantic Ridge (NMAR). The red star makes the location of the TAG Vent



creates an object containing all the video data. The video data were then converted into consecutive color RGB images at a frame rate of 1/29.97 s between consecutive frames using the Matlab function *imwrite*. For each investigated site, we typically obtained an image sequence of 300–600 still images. Next, the color RGB images were converted into grayscale images using the Matlab function *rgb2gray*. Finally, contrast of the grayscale frames was enhanced by using the contrast-limited adaptive histogram equalization method and the Matlab function *adapthisteq* (Zuiderveld 1994) to highlight the zones of flowing fluid.

Particle image velocimetry (PIV)

The particle image velocimetry (PIV) method has been commonly used in the study of fluid dynamics including buoyant plumes (Prasad 2000; Adrian 2005; Pham et al. 2005; Westerweel et al. 2013; Zhang et al. 2017). Here, we applied the PIV method to analyze in-situ video image sequences of hydrothermal plumes to retrieve quantitative information on plume velocity fields. PIV tracks the motion of tracer particles in a flow field over a small time interval and calculates the instantaneous flow velocity field using a spatial cross-correlation method (Prasad 2000). Hydrothermal plumes

are embedded with precipitated particles, fluid parcels, and smoke billows owing to plume interactions with the ambient seawater (Fig. 2). In this study, we used these distinctly visible features as tracers to estimate the hydrothermal plume flow.

In our study, we used a multi-pass PIV method with successively decreasing interrogation window sizes (<http://www.lavision.de/en/products/davis.php>) and calculated the velocities of turbulent fluid parcels from the time series images of hydrothermal plumes. The interrogation window sizes of the initial and final step were 64 × 64 pixels and 32 × 32 pixels, respectively, with an overlap of 50%.

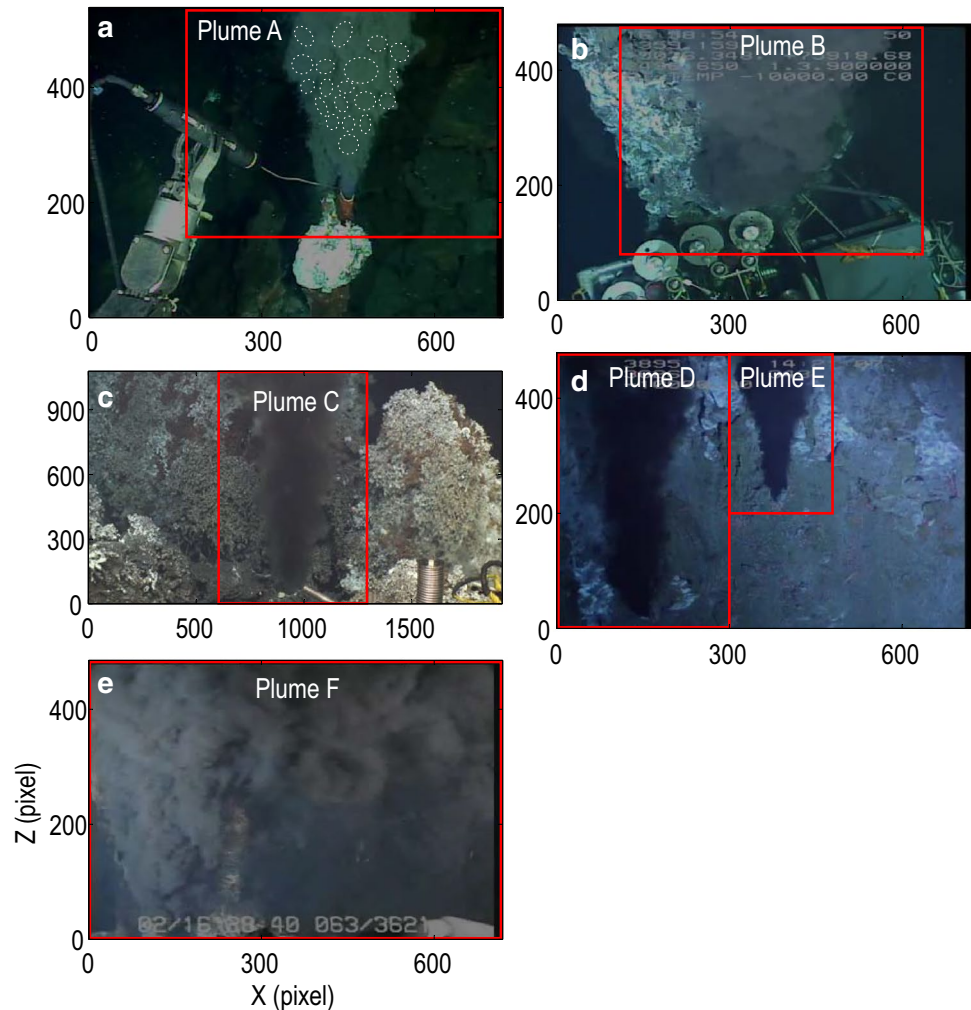
Results

Characteristics of hydrothermal plumes

Turbulent parcels

Turbulent fluid parcels of different scales were clearly visible within rising plumes (Fig. 2). The outlines of turbulent parcels within the V Vent plumes at the EPR show that the radii of these turbulent parcels ranged from tens to hundreds

Fig. 2 Video images of six hydrothermal plumes (Plumes A–F) at different mid-ocean ridges. The red boxes show the areas in which the particle image velocimetry (PIV) method was applied. **a** Image captured from the video of the V Vent located at the EPR. The white dotted ellipses mark the boundaries of a subset of identifiable turbulent parcels. **b** Image captured from the video of the Biotransect Vent located at the EPR. **c** Image captured from the video of the Main Endeavour Field located at the JdFR. **d, e** Images captured of three plumes from the videos of the TAG Vent located at the NMAR



of pixels (Fig. 2a). Through coalescing with adjacent parcels and interacting with the ambient water column, scales of these turbulent parcels changed rapidly. Turbulent parcels with apparent high fluxes were observed to occur periodically within all six studied plumes (Online supplementary material—video clips of six studied plumes). Moreover, Plumes A, B and F are more vigorous than Plumes C, D and E as viewed from the video clips (Fig. 2).

Plume width

The cross-sectional dimension of a near-bottom hydrothermal plume was observed to increase 3–9 times within an upwelling distance of hundreds of pixels (Fig. 2), indicating rapid entrainment of the ambient fluids into the rising plume.

Other features

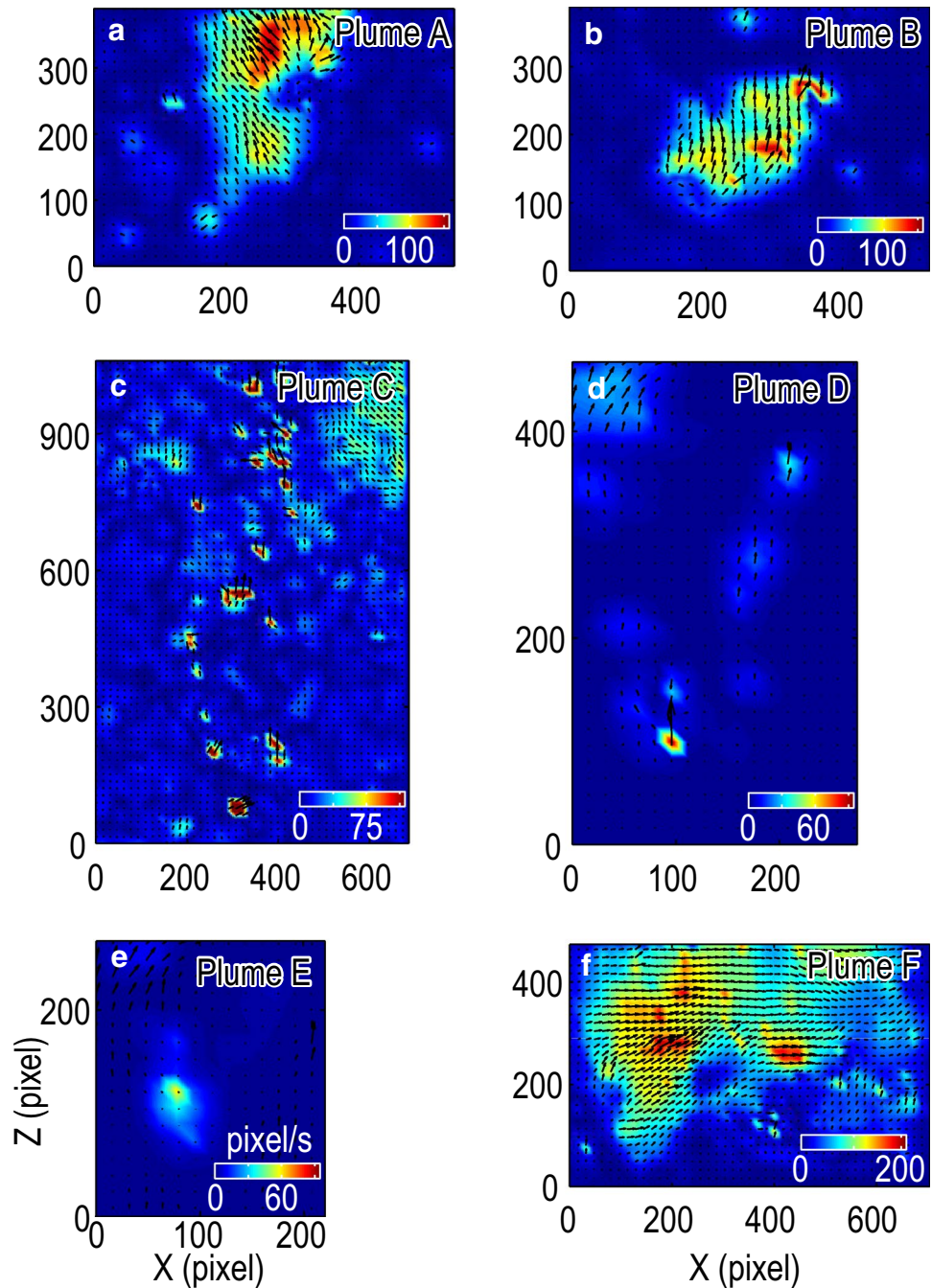
Two originally separated plumes were observed to merge at about 150 pixels (30 cm) above the vent orifice (Fig. 2a). A rising plume was also observed to spread laterally at about 250 pixels above the vent orifice (Fig. 2e).

Velocity field

Instantaneous velocity field

In this study, the instantaneous velocity fields calculated by the PIV revealed the apparent motion of turbulent parcels instead of individual particles (Fig. 3). The outlines of these velocity fields agreed well with the plume boundaries, which were identified by the higher concentration of optically visible particles relative to the background. The detailed turbulent structures of plumes cannot be seen clearly from these velocity fields. Due to lateral spreading,

Fig. 3 Instantaneous velocity fields of the hydrothermal plumes (Plumes A–E) calculated by the PIV method



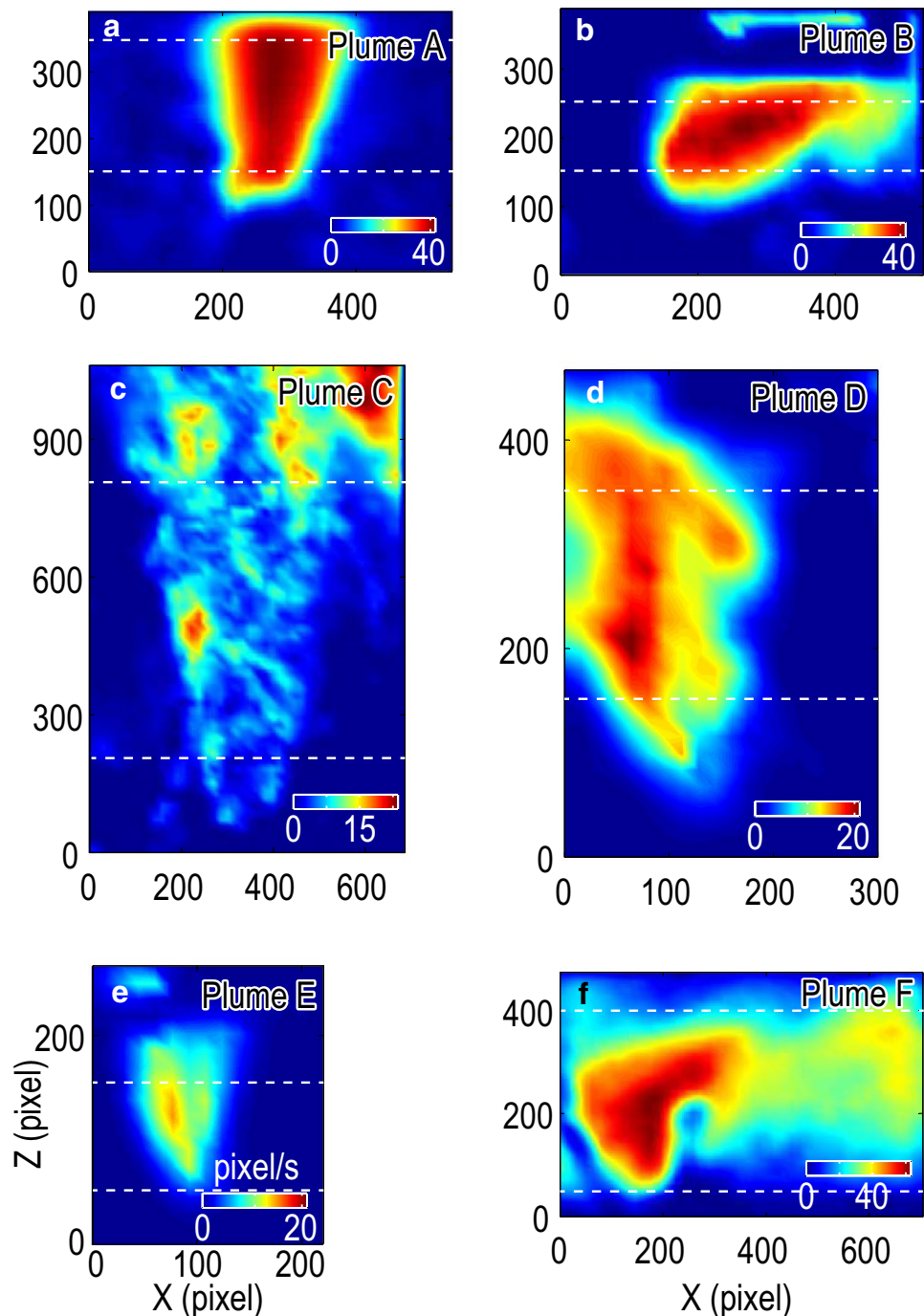
a considerable horizontal component was observed in the instantaneous velocity field of Plume F (Fig. 3f).

Mean vertical velocity field

The temporally averaged mean vertical velocity field reached its maximum speed at the plume centerline, gradually reduced to almost zero at the plume boundary, and completely vanished outside the plume (Fig. 4). Because of the edge effects at the image boundaries or the printed

labels in the upper part of images tending to smear the image intensities (Fig. 2), the mean vertical velocities at the top of image frames were cut off to zero (Fig. 4). However, lateral spreading also contributed to decreasing the mean vertical velocity at the top of image frames of Plume F (Fig. 4f). For Plume C, the mean vertical velocity reached its maximum at the plume boundary (Fig. 4c) as the turbulent parcels were only observed clearly at the plume edge (Fig. 2c).

Fig. 4 Mean vertical velocity field of the hydrothermal plumes (Plumes A–E). For Plume C, the mean vertical velocity reaches its maximum at the plume’s boundary because the turbulent parcels are only clearly visible at the plume’s boundary (Fig. 2c). The dashed line delimits the area where the vertical flux and the power spectrum density are estimated



Entrainment coefficient

The horizontal profiles of the mean vertical velocity $w(x, z)$ and mean particle concentration $c(x, z)$ at any given height z are assumed to be self-similar and therefore can be represented by Gaussian curves (Morton et al. 1956; Turner 1986):

$$w(x, z) = w_c(z) e^{-\frac{x^2}{b_w^2}} \quad (1)$$

$$c(x, z) = c_c(z) e^{-\frac{x^2}{b_c^2}} \quad (2)$$

where $w_c(z)$ and $c_c(z)$ are the mean vertical velocity and mean particle concentration at the plume centerline, respectively. The radial scale $b(z)$ is the distance from the plume centerline to the point where the mean plume vertical velocity or the mean particle concentration reduces to $1/e$ of that at the

plume centerline at a given height z . The variable b can be inverted by a linear fitting function of z :

$$b = cz + b_0 \tag{3}$$

For hydrothermal plumes (Morton et al. 1956; Turner 1986), the coefficient c can be written as follows:

$$c = \frac{6}{5}\alpha \tag{4}$$

where α is the Gaussian entrainment coefficient, which can be defined as the ratio between the mean inflow velocity at the edge of the plume and the mean vertical velocity at the centerline of the plume (Morton et al. 1956; Turner 1986).

The horizontal profiles of the mean vertical velocity over a certain height range agree well with the fitted Gaussian curves (Fig. 5). In general, the radial scale b , which characterizes the plume width, increases with increasing height

above the vent orifice and can be fitted into a linear function of z (Fig. 6). However, for the mean vertical velocity profiles, the height variations of the plume width b have relatively large misfits for Plumes C and F (light pink dotted line in Fig. 6c, f, respectively). The entrainment coefficients α_w estimated for Plumes A–F are 0.21, 0.32, 0.21, 0.16, 0.16, and 0.31, respectively (Table 1). These entrainment coefficients (0.16–0.32) exceed the range of Gaussian entrainment coefficients (0.07–0.12) that were derived for buoyant plumes by previous experiments (Papanicolaou and List 1988; Wang and Law 2002; Zhang et al. 2017) and numerical simulations (Jiang and Breier 2014).

We also used the horizontal profiles of the mean image intensity to estimate the entrainment coefficients (α_θ), assuming that the image intensity represents particle concentration in the plume. The horizontal profiles of the mean image intensity agreed well with the fitted Gaussian curves

Fig. 5 Horizontal profiles of the mean vertical velocities (red lines) and the mean image intensities (black lines) for Plumes A–E. Corresponding best-fitting Gaussian curves are shown for the mean vertical velocity profile (dashed red lines) and mean image intensities (black dashed lines)

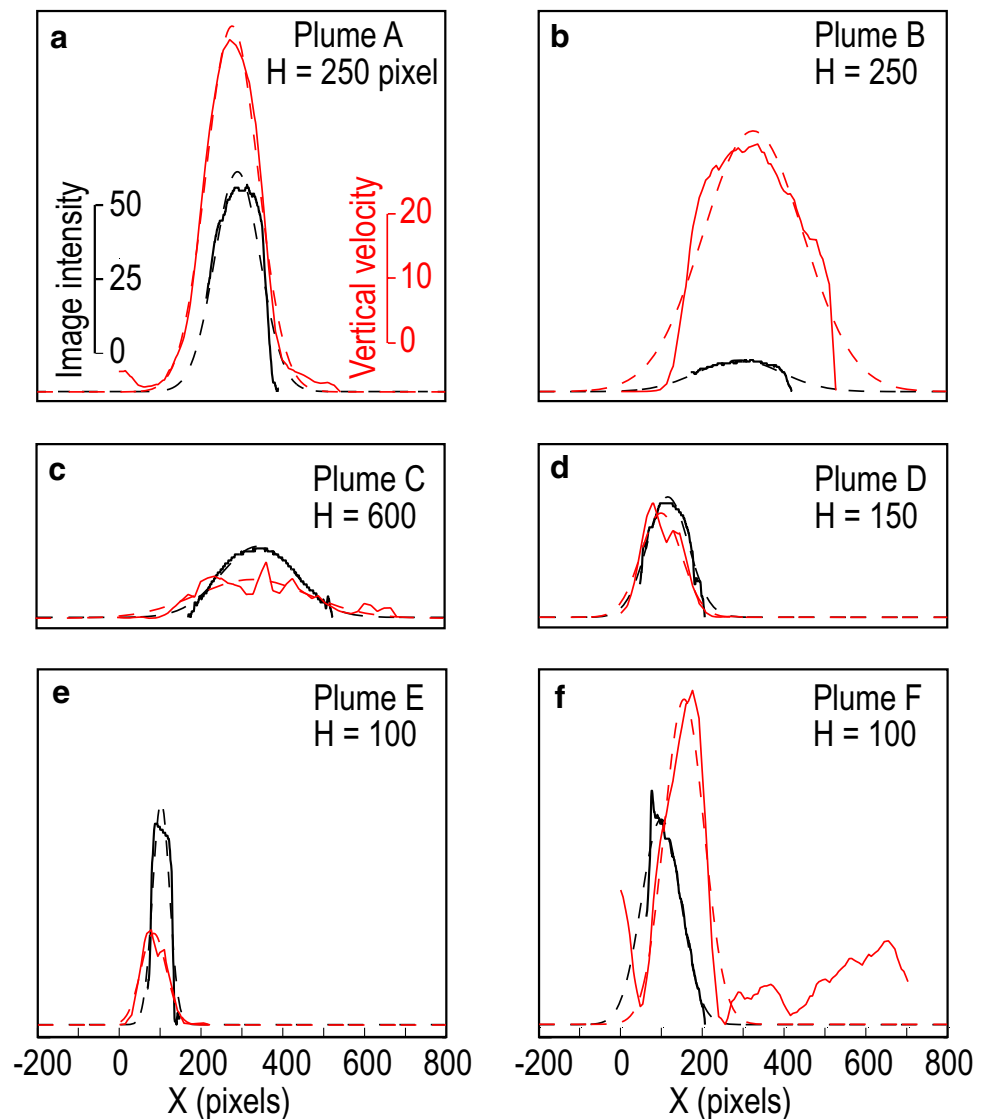


Fig. 6 Height variation in the plume mean characteristic width b identified by velocity profiles (red lines) and image intensity profiles (black lines) using Eq. (1) as a function of height above the vent orifice. Also shown are the corresponding best-fitting linear trend (dashed lines). The entrainment coefficients α_w and α_θ are calculated using Eq. (2). Note that the image intensity profiles for Plume B (gray dotted line) has relatively large misfit to the linear trend, while the vertical velocity profiles for Plumes C and F (light pink dotted lines) have relatively large misfits

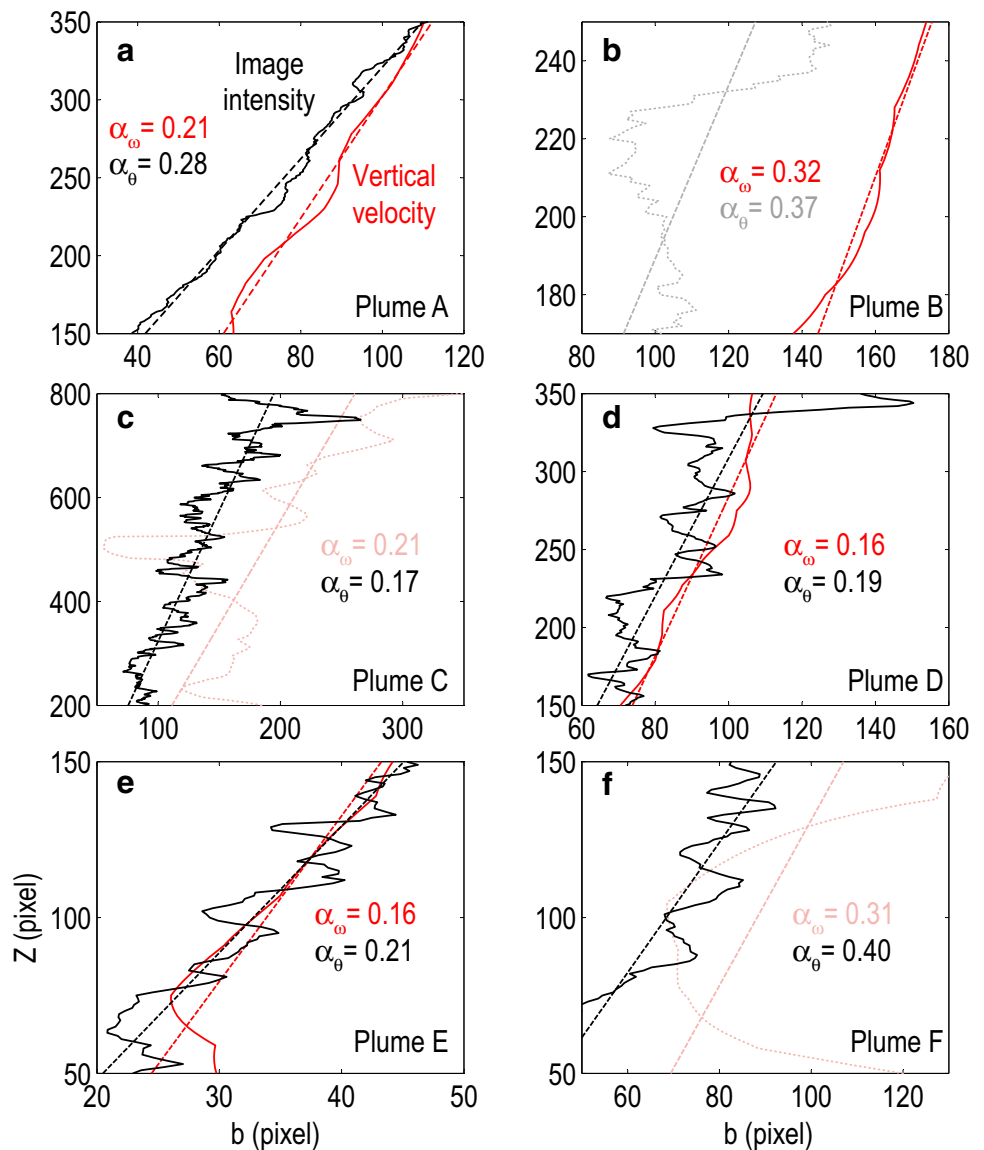


Table 1 Entrainment coefficients

Plume No.	Intensity entrainment coefficient α_θ	Velocity entrainment coefficient α_ω	Ratio between α_θ and α_ω	Deviations from empirical value ($\lambda_0=1.2$) (%)
Plume A	0.28	0.21	1.33	10.8
Plume B	0.37*	0.32	1.16	-3.3
Plume C	0.17	0.21*	0.81	-32.5
Plume D	0.19	0.16	1.19	-0.8
Plume E	0.21	0.16	1.31	9.2
Plume F	0.40	0.31*	1.29	7.5

*Indicates cases where the relationships between plume width and plume height have relatively large misfits to the linear trend

(Fig. 5). In general, the radial scale b of the mean image intensity profile also increases with increasing height above the vent orifice and were fitted into a linear function of z

(Fig. 6). However, for the image intensity profiles, the height variations of the plume width b have relatively large misfits for Plume B (gray dotted line in Fig. 6b). The estimated

entrainment coefficients α_θ are 0.28, 0.37, 0.17, 0.19, 0.21, and 0.40 for Plumes A–E, respectively (Table 1). Thus the above analyses imply that the results for Plumes A, D, and E might be the most robust, while Plumes B, C, and F might be associated with larger uncertainties.

Spatial variations in the vertical flux

The mean vertical flux increased with increasing height above the vent orifice and varied greatly for different plumes (Fig. 7Aa, Ba, Ca, Da, Ea, Fa). Considering the relatively large uncertainties in the plume width-height relationships (as shown in Fig. 6) for Plumes B, C, and F, these three plumes are shown by light gray shades in Fig. 7. Overall, the mean fluxes of Plumes A, B and F are greater than those of Plumes C, D and E at the same height above the vent orifice (e.g., 100 pixels above the vent orifice, Fig. 7), which is consistent with the vigor of plume flows viewed from the videos (Fig. 2). At 200 mm above the vent orifice, the vertical flux of Plume A is $3.3 \times 10^4 \text{ mm}^2/\text{s}$, which is greater than that of Plume C of $497 \text{ mm}^2/\text{s}$. However, due to the lack of

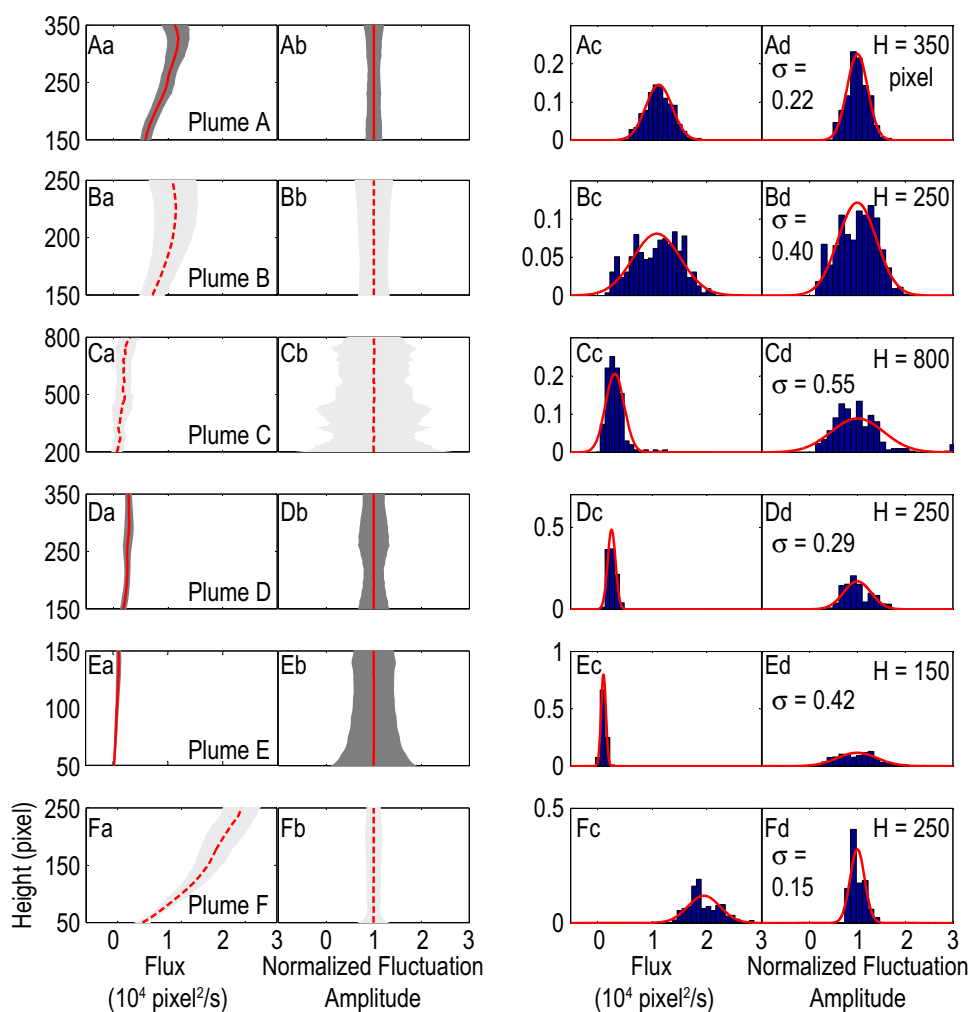
reference length scales (e.g., a temperature probe or laser beam scale) for Plumes B, D, E and F, we only obtained the relative values of vertical fluxes for these plumes in unit of pixel^2/s . The distributions of plume vertical fluxes can be fitted relatively well by Gaussian curves (Fig. 7Ac, Bc, Cc, Dc, Ec, Fc).

To estimate the relative variations of the vertical fluxes, we normalized the vertical flux and its standard deviation by the mean vertical flux at the same height above the vent orifice (Fig. 7Ab, Ba, Ca, Da, Ea, Fa). The resultant 1- σ values of the normalized fluctuation amplitude were relatively stable along the vertical axis and ranged from 15 to 55% at the selected heights (Fig. 7Ad, Bd, Cd, Dd, Ed, Fd).

Temporal fluctuations in the vertical flux

The time series of the vertical flux (Fig. 8) were obtained by horizontally integrating the profiles of instantaneous vertical velocity. We focused on certain height ranges delimited by white dashed lines in Fig. 4 to investigate temporal plume fluctuations to reduce the edge effect. Moreover, in order to

Fig. 7 Variations of the mean vertical fluxes and the normalized fluctuation amplitude as a function of the height above the vent orifice. Shaded gray areas show the temporal 1- σ variations of the vertical fluxes (left column) and the normalized fluctuation amplitude (second left column), defined as the temporal range of plume width normalized by the mean plume vertical flux. Because of the relatively large misfits to the linear trends in the image intensity or vertical velocity profiles for Plumes B, C, and F (i.e., Fig. 6), these plumes are marked in light gray shades. The corresponding Gaussian distributions at the selected heights are shown for mean vertical flux (third column) and the normalized fluctuation amplitude (right column)



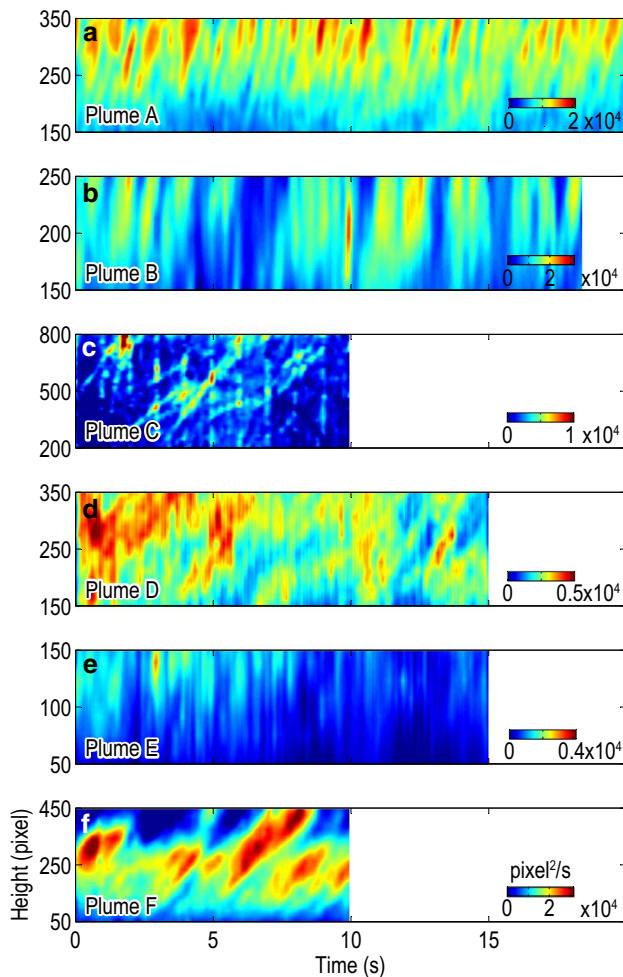


Fig. 8 The time series of vertical fluxes

reduce the random noise, we smoothed the vertical flux time series using a moving-average filter (Fig. 8). The period of the averaging window is 1/6 s, and the window is moved from left to right along the time axis in 1/30 s increments.

Periodic fluctuations can be seen in the plume vertical flux time series (Fig. 8). The dominant periods of the vertical flux oscillations of all six studied plumes are limited in a narrow band of 0.5–5 s (Fig. 9). In order to identify the dominant oscillation periods, we selected several profiles from the plume vertical flux time series (Fig. 10). Temporal oscillations in the vertical flux are clearly present and amplitudes of the vertical flux vary greatly for different hydrothermal plumes from 5×10^3 to 3×10^4 pixel²/s (Fig. 10Aa, Ba, Ca, Da, Ea, Fa). The dominant periods for Plume A (Fig. 2a) are 0.5, 1.8 and 3.3 s (Fig. 10Ab). Similarly, the dominant periods are in the range of 0.5–5 s for the other five plumes (Fig. 10Bb, Cb, Db, Eb, Fb).

The periods with the greatest energy for Plumes A–F are 1.8, 4.6, 2.9, 4.9, 5.0 and 2.9 s, respectively (Fig. 10Ab, Bb, Cb, Db, Eb, Fb). The period t and normalized

fluctuation amplitude A appear to be correlated for all plumes except for Plume C (Fig. 11).

Discussion

Comparison of two entrainment coefficients

The two entrainment coefficients, α_θ and α_w , are related by

$$\alpha_\theta = \lambda \alpha_w \quad (5)$$

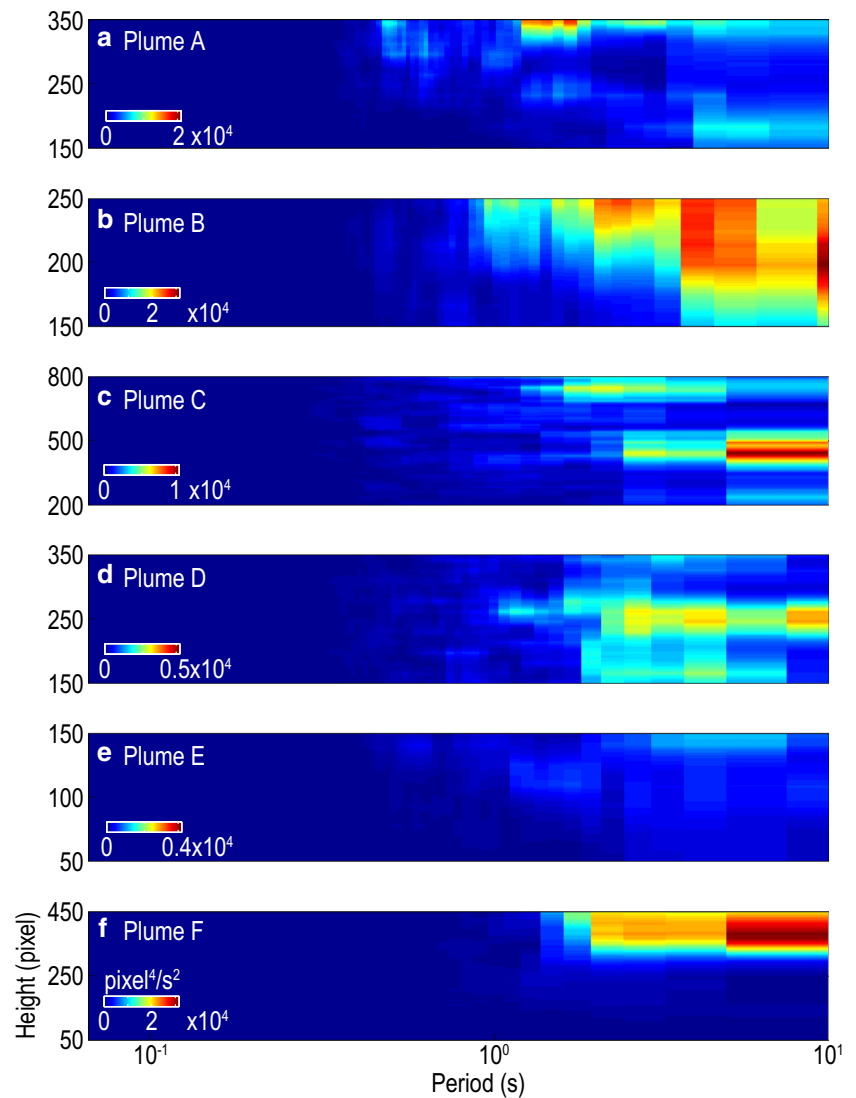
where λ is the concentration-to-velocity width ratio, which is ~ 1.2 (Turner 1986; Rona et al. 2006). The ratios between the two entrainment coefficients estimated in our study are 0.81–1.33, and the deviations from the empirical value ($\lambda = 1.2$) are less than 11% for the five studied plumes (Table 1). However, for Plume C the ratio $\lambda = 0.81$ and the deviation is approximately -32.5% due to the mean vertical velocity reaching its maximum at the plume boundary (Fig. 4c). Considering the uncertainties in the two methods, the entrainment coefficients are consistent with each other.

Error analysis

Several factors may have contributed to the errors in the instantaneous velocity fields calculated by the PIV method. First, the unknown viewing angle of the video camera towards the plume may have caused under-estimation or over-estimation of the velocities. Second, the 2-D projection of a 3-D cone-shaped turbulent plume may have obscured the high-velocity core (e.g., Karlstrom et al. 2013). Third, the limited spatial resolution of image intensity and the relatively low frame rate may have added uncertainties to the calculation of the velocity field when there were no identifiable flow features in one or both consecutive frames or when flow features changed rapidly (e.g., Crone et al. 2008). Finally, the inherent bias of the PIV method may have under-estimated the velocity fields and flow rates (Crone et al. 2008; McNutt et al. 2012).

Although the entrainment coefficients were over-estimated by the two methods using either the mean vertical velocity or the mean image intensity, both methods generated consistent results, indicating that the present PIV method under-estimated the plume velocity field proportionally over the whole domain. Thus, the variations or relative changes of the flow rates estimated by the PIV method were more accurate than the absolute values. Similar methods have been used to investigate tidal oscillations of hydrothermal plume velocities (Mittelstaedt et al. 2016) and oscillations in geyser eruption rates (Karlstrom et al. 2013).

Fig. 9 The power spectrum densities of the time series of vertical fluxes



Probable causes for the observed short-period variations in vertical fluxes

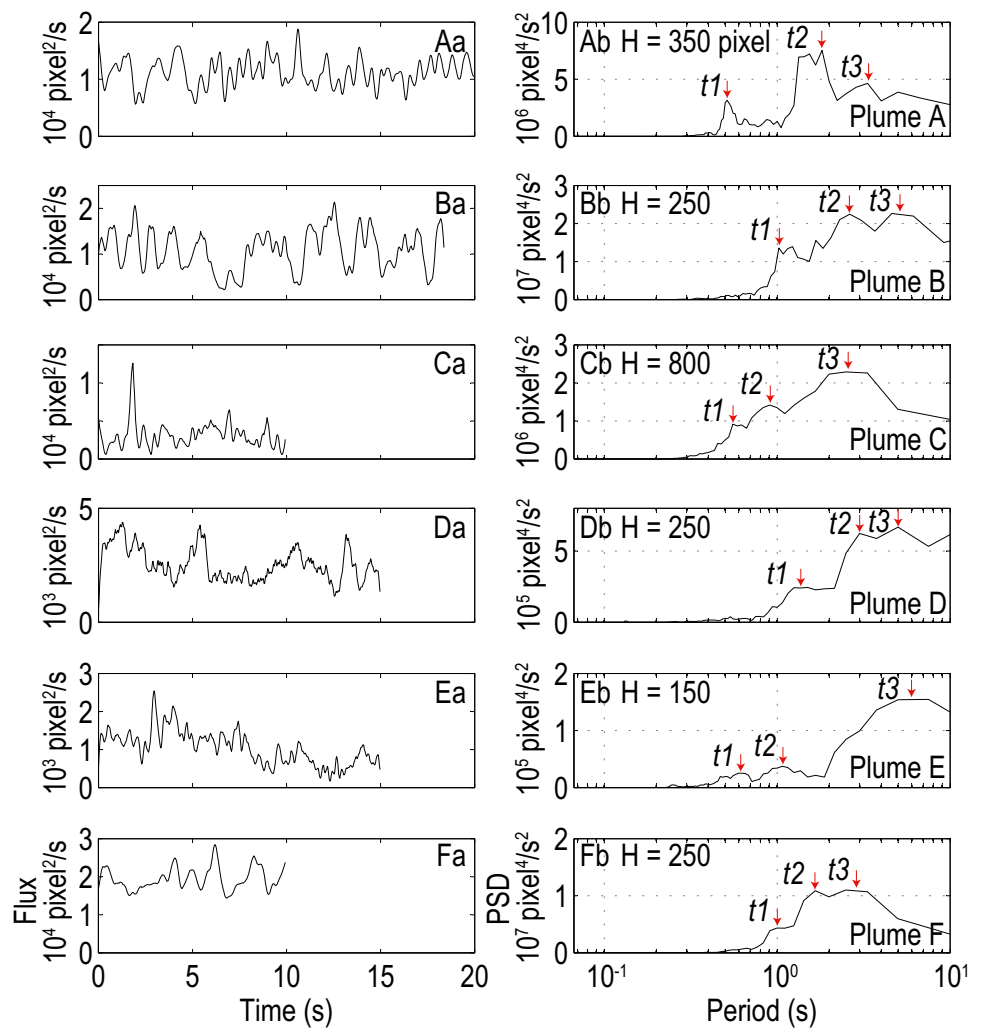
The flow dynamic instability of two-phase fluid, i.e., pressure-drop instabilities, within hydrothermal systems might explain the observed plume flux oscillations of 0.5–5 s periods. Flow instabilities were widely observed in geyser eruption (Karlstrom et al. 2013) and in lava dome growth and eruption (Voight et al. 1999; Denlinger and Hoblitt 1999; Kozono and Koyaguchi 2012).

Inside the hydrothermal systems at mid-ocean ridges, hot seawater fluid ascends adiabatically while heated by axial magma lenses. If intersecting the two-phase boundary of seawater, the ascending hot fluid will experience subcritical or supercritical phase separation, resulting in the production of a low salinity vapor phase and a high salinity brine phase (e.g., Delaney et al. 1987; Von Damm and Bischoff 1987; Cowan and Cann 1988; Von Damm 1988; Bischoff

and Rosenbauer 1989; Butterfield et al. 1990; Nehlig 1991; Kelley et al. 1992, 1993; Saccocia and Gillis 1995). For the same vent fields as those investigated in our study, phase separation was proposed to account for the variations in chemistry of hydrothermal fluids (Edmond et al. 1995; Oosting and Von Damm 1996; Seyfried et al. 2003). Previous studies have shown that fluid temperatures for the hydrothermal plumes at the EPR and JdFR were just around the seawater boiling curve (Hannington et al. 2005), indicating that two-phase fluids might exist at shallow depth beneath the vent orifice. In contrast, fluid temperatures for the studied plumes at the NMAR were below the two-phase boundary (Hannington et al. 2005), indicating that two-phase fluids might exist at greater depth beneath the vent orifice.

Previous studies have shown that pressure-drop type of oscillations could be induced in a chamber of a mixed fluid and compressible vapors (Stenning 1964; Kakac and Bon 2008; Chiapero et al. 2012; Ruspini et al. 2014).

Fig. 10 Selected profiles of the vertical fluxes (left column) and the related power spectrum densities (right column). The dominant periods are marked by red arrows



According to Fig. 12, the following steady-state relations are considered:

$$P_i - P_0 = K_1 Q_1^2 \quad (6)$$

$$P_0 - P_e = f(Q_2) \quad (7)$$

where P_i is the pressure in the fluid supply zone below the compressible gas chamber, P_0 is the pressure in the compressible gas chamber, P_e is the pressure at the vent orifice, K_1 is an experimentally-determined constant for the inlet restriction, Q_1 is the flow rate into the chamber and Q_2 is the flow rate out of the chamber. P_i and P_e are assumed to be constant. Under certain conditions, the curve of the pressure drop as a function of Q_2 may follow an N-shaped path (Fig. 12b). When the slope of the curve of pressure drop as a function of Q_1 is steeper than that corresponding to Q_2 , an oscillation could occur. The mechanism of pressure-drop oscillation can be explained in Fig. 12b. If the two curves are intersected where the slope of pressure drop as a function of Q_1 is more negative than that corresponding to Q_2 ,

a small increase in P_0 will cause Q_2 to decrease more than Q_1 , indicating that more fluid enters the compressible gas chamber than that leaves it. Thus, the chamber pressure P_0 increases. The state of the fluid moves up until it reaches the peak B. Then a flow excursion from a two-phase state to a liquid state could occur from B to C. At C, the amount of fluid leaving the chamber is more than that entering it. Hence, a decompression process takes place in the chamber from C to D, where the state of the fluid reaches the curve minima. Then a flow excursion from the liquid-phase dominated two-phase state to the vapor-phase dominated two-phase state could occur from D to (A). At this point, the fluid entering the chamber is more than that leaving it. Hence, a compression process occurs in the chamber from A to (B). Thus, the limit cycle A–B–C–D–A represents a fully developed pressure-drop oscillation.

Model results predict that shorter periods and smaller amplitude of pressure-drop oscillations could result from increasing flow rate, increasing inlet fluid temperature, or decreasing reservoir compressibility (Kakaç et al. 1990;

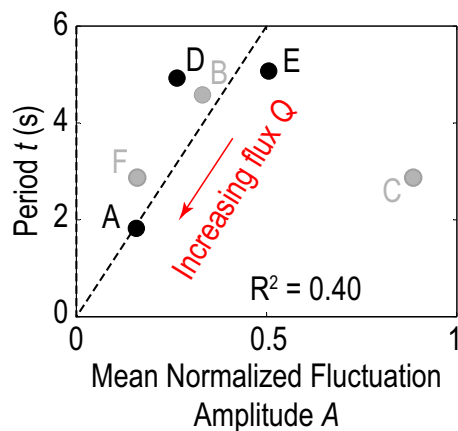


Fig. 11 The relationship between oscillation period t and mean normalized fluctuation amplitude A . The linear trend (black dashed line) was constrained by Plumes A, D and E because of the robust relationship between plume width and height for the three plumes. The correlation coefficient is $R^2=0.40$ for Plumes A, D, and E. If Plumes B and F are also included, $R^2=0.38$. With increasing flux Q , the period and fluctuation amplitude are expected to decrease (red arrow). The normalized fluctuation amplitude for each plume is averaged over a certain height range, which is similar with those in Fig. 7

Liu and Kakac 1991; Padki et al. 1991; Chiapero et al. 2012). The normalized fluctuation amplitude A in our study represents the amplitude of flux oscillation deviating from the mean value. The observed oscillation period t and the mean fluctuation amplitude A show general correlation for Plumes A, D, and E as predicted by the theoretical models (Fig. 11), while Plumes B and F also seem to fit this trend. As plume flux Q increases, both the oscillation period t and oscillation amplitude A are expected to decrease (red arrow in Fig. 11). Thus the oscillation characteristics for most of the plumes, especially Plumes A, D, and E, which have the robust relationship between plume width and height, seem to be consistent with the model predictions.

Previous studies have observed a wide range of oscillation periods in the seafloor hydrothermal plume processes from changes in acoustic energy (0.004–0.1 s; Crone et al. 2006) to hydrothermal microseismicity (0.07–0.33 s; Sohn et al. 1995), to changes in ocean bottom pressure (22–53 min; Sohn et al. 2009), and to changes in flow rate, temperature, and chemicals (~12 h; e.g., Little et al. 1988; Schultz et al. 1996; Tivey et al. 2002; Scheirer et al. 2006; Larson et al. 2007, 2009; Crone et al. 2010; Xu et al. 2013, 2017; Barryre et al. 2014; Mittelstaedt et al. 2016) (Fig. 13). The results of this study have added a unique new window of 0.5–5 s in the spectrum of oscillation periods. More importantly, the relatively narrow band width of the observed oscillation periods of plumes at three ridges might reflect strong common features in plume dynamics despite the diverse geological settings of the studied plumes.

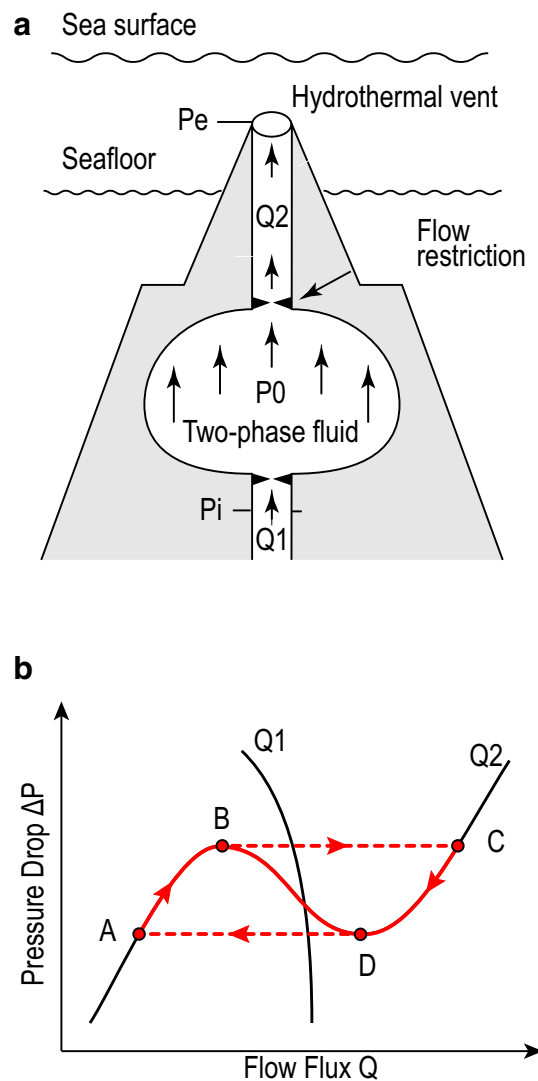


Fig. 12 Schematics illustrating the hypothesized mechanism of pressure-drop oscillation. **a** Schematic illustration of conduit flow for hydrothermal vent eruption. **b** Characteristic curves for pressure-drop and flow flux and the limit cycle of pressure-drop oscillation

Conclusions

The main conclusions of this study include the following:

- (1) Turbulent parcels of different scales were observed to occur periodically within plumes.
- (2) The entrainment coefficients estimated by either the mean image intensity or the mean vertical velocity were consistent with each other, with a mean value of the intensity-to-velocity width ratio of ~1.2 as predicted by theoretical model.
- (3) The mean vertical flux was observed to increase with increasing height above the vent orifice. The temporal 1- σ standard variation of the vertical flux was in the

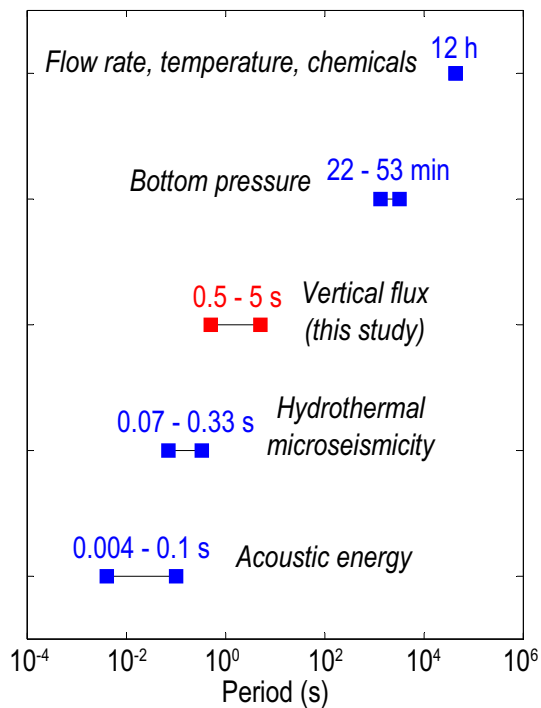


Fig. 13 Comparisons of processes with different observed oscillation periods in seafloor hydrothermal systems. The periods of acoustic energy were identified by Crone et al. (2006). The periods of hydrothermal microseismicity were observed by Sohn et al. (1995). The periods of bottom pressure were provided by Sohn et al. (2009). In addition, long-term observations have also shown 12-h oscillations for flow rate, temperature and chemicals of hydrothermal fluids (e.g., Little et al. 1988)

range of 15–55% of the mean vertical flux, indicating significant dispersion of the turbulent parcels in the rising plume.

- (4) Short-period oscillations of 0.5–5 s were observed in plume vertical fluxes. The observed oscillation period t and the mean fluctuation amplitude A show correlation, both might increase with decreasing mean vertical flux. It is hypothesized that the short-period oscillations might be caused by the pressure-drop oscillation within a network of compressible two-phase fluid within a sub-seafloor hydrothermal source reservoir.

Acknowledgements We are grateful to Dr. Jian Zhu for providing technical assistance and Dr. Guangyu Xu for providing the plume videos recorded at the JdFR. This work was supported by the Ministry of Science and Technology 973 Project (2012CB417303), the National Natural Science Foundation of China (91628301, U1606401), the Chinese Academy of Sciences (Y4SL021001, QYZDY-SSW-DQC005), the Chinese National 985 Project (1350141509), the International Exchange Program for Graduate Students, Tongji University (201502) and the Chinese Scholarship Council (201606260207). H.J. was supported by a National Science Foundation Grant NSF OCE-1038055 through the RIDGE2000 program.

References

- Adrian RJ (2005) Twenty years of particle image velocimetry. *Exp Fluids* 39:159–169
- Baker ET (2007) Hydrothermal cooling of midocean ridge axes: do measured and modeled heat fluxes agree? *Earth Planet Sci Lett* 263:140–150
- Barreyre T, Sohn RA (2016) Poroelastic response of mid-ocean ridge hydrothermal systems to ocean tidal loading: implications for shallow permeability structure. *Geophys Res Lett* 43:1660–1668
- Barreyre T, Escartín J, Sohn RA, Cannat M, Ballu V, Crawford WC (2014) Temporal variability and tidal modulation of hydrothermal exit-fluid temperatures at the Lucky Strike deep-sea vent field, Mid-Atlantic Ridge. *J Geophys Res* 119:2543–2566
- Bischoff JL, Rosenbauer RJ (1989) Salinity variations in submarine hydrothermal systems by layered double-diffusive convection. *J Geol* 97:613–623
- Butterfield DA, Massoth GJ, McDuff RE, Lupton JE, Lilley MD (1990) Geochemistry of hydrothermal fluids from Ashes Vent Field, Axial Seamount, Juan de Fuca Ridge: seafloor boiling and subsequent fluid-rock interaction. *J Geophys Res* 95:895–12922
- Carbotte SM et al (2004) New integrated data management system for Ridge2000 and Margins Research. *EOS Trans AGU* 85:553–559
- Chiapero EM, Fernandino M, Dorao CA (2012) Review on pressure drop oscillations in boiling systems. *Nucl Eng Des* 250:436–447
- Converse DR, Holland HD, Edmond JM (1984) Flow rates in the axial hot springs of the East Pacific Rise (21°N): implications for the heat budget and the formation of massive sulfide deposits. *Earth Planet Sci Lett* 69:159–175
- Corliss JB et al (1979) Submarine thermal springs on the Galápagos Rift. *Science* 203:1073–1083
- Cowan J, Cann J (1988) Supercritical two-phase separation of hydrothermal fluids in the Troodos ophiolite. *Nature* 333:259–261
- Crone TJ, Wilcock WSD, Barclay AH, Parsons JD (2006) The sound generated by mid-ocean ridge black smoker hydrothermal vents. *PLoS ONE* 1:e133
- Crone TJ, McDuff RE, Wilcock WSD (2008) Optical plume velocimetry: a new flow measurement technique for use in seafloor hydrothermal systems. *Exp Fluids* 45:899–915
- Crone TJ, Wilcock WSD, McDuff RE (2010) Flow rate perturbations in a black smoker hydrothermal vent in response to a mid-ocean ridge earthquake swarm. *Geochem Geophys Geosyst* 11:Q03012
- Delaney JR, Mogk DW, Mottl M (1987) Quartz-cemented breccias from the Mid-Atlantic Ridge: samples of a high-salinity hydrothermal upflow zone. *J Geophys Res* 92:9175–9192
- Denlinger RP, Hoblitt RP (1999) Cyclic eruptive behavior of silicic volcanoes. *Geology* 27:459–462
- Edmond J et al (1995) Time series studies of vent fluids from the TAG and MARK sites (1986, 1990). In: Parson LM, Walker CL, Dixon DP (eds) *Hydrothermal vents and processes. Mid-Atlantic Ridge: a new solution chemistry model and a mechanism for Cu/Zn zonation in massive sulphide orebodies*, vol 87. Geological Society, London, pp 77–86
- Elderfield H, Schultz A (1996) Mid-ocean ridge hydrothermal fluxes and the chemical composition of the ocean. *Annu Rev Earth Planet Sci* 24:191–224
- Escartín J, Garcia R, Barreyre T, Cannat M, Gracias N, Shihavuddin A, Mittelstaedt E (2013) Optical methods to monitor temporal changes at the seafloor: the Lucky Strike deep-sea hydrothermal vent field (Mid-Atlantic Ridge). In: *Underwater Technology Symposium (UT)*, 2013 IEEE International, Tokyo, Japan
- German CR, Von Damm KL (2006) Hydrothermal processes. In: Elderfield H, Holland H, Turekian K (eds) *Treatise on geochemistry*, vol 6. Elsevier, Amsterdam, pp 181–222

- Germanovich LN, Hurt RS, Smith JE, Genc G, Lowell RP (2015) Measuring fluid flow and heat output in seafloor hydrothermal environments. *J Geophys Res* 120:8031–8055
- Ginster U, Mottl MJ, Von Herzen RP (1994) Heat flux from black smokers on the Endeavour and Cleft segments, Juan de Fuca Ridge. *J Geophys Res* 99:4937–4950
- Hannington MD, de Ronde CEJ, Petersen S (2005) Sea-floor tectonics and submarine hydrothermal systems. In: Hedenquist JW, Thompson JFH, Goldfarb RJ, Richards JP (eds) *Economic geology 100th anniversary volume*. Society of Economic Geologists, Littelton, pp 111–141
- Jackson DR, Jones CD, Rona PA, Bemis KG (2003) A method for Doppler acoustic measurement of black smoker flow fields. *Geochem Geophys Geosyst* 4:1095
- Jiang H, Breier JA (2014) Physical controls on mixing and transport within rising submarine hydrothermal plumes: a numerical simulation study. *Deep-Sea Res I* 92:41–55
- Kadko D (1993) An assessment of the effect of chemical scavenging within submarine hydrothermal plumes upon ocean geochemistry. *Earth Planet Sci Lett* 120:361–374
- Kakac S, Bon B (2008) A Review of two-phase flow dynamic instabilities in tube boiling systems. *Int J Heat Mass Transfer* 51:399–433
- Kakaç S, Veziroğlu TN, Padki MM, Fu LQ, Chen XJ (1990) Investigation of thermal instabilities in a forced convection upward boiling system. *Exp Therm Fluid Sci* 3:191–201
- Karlstrom L et al (2013) Eruptions at Lone Star Geyser, Yellowstone National Park, USA: 1. Energetics and eruption dynamics. *J Geophys Res* 118:4048–4062
- Kelley DS, Robinson PT, Malpas JG (1992) Processes of brine generation and circulation in the oceanic crust: fluid inclusion evidence from the Troodos Ophiolite, Cyprus. *J Geophys Res* 97:9307–9322
- Kelley DS, Gillis KM, Thompson G (1993) Fluid evolution in submarine magma-hydrothermal systems at the Mid-Atlantic Ridge. *J Geophys Res* 98:19579–19596
- Kozono T, Koyaguchi T (2012) Effects of gas escape and crystallization on the complexity of conduit flow dynamics during lava dome eruptions. *J Geophys Res* 117:B08204
- Larson BI, Olson EJ, Lilley MD (2007) In situ measurement of dissolved chloride in high temperature hydrothermal fluids. *Geochim Cosmochim Acta* 71:2510–2523
- Larson BI, Lilley MD, Olson EJ (2009) Parameters of subsurface brines and hydrothermal processes 12–15 months after the 1999 magmatic event at the Main Endeavor Field as inferred from in situ time series measurements of chloride and temperature. *J Geophys Res* 114:B01207
- Little SA, Stolzenbach KD, Grassle FJ (1988) Tidal current effects on temperature in diffuse hydrothermal flow: Guaymas Basin. *Geophys Res Lett* 15:1491–1494
- Liu H, Kakac S (1991) An experimental investigation of thermally induced flow instabilities in a convective boiling upflow system. *Heat Mass Transfer* 26:365–376
- Macdonald KC, Becker K, Spiess FN, Ballard RD (1980) Hydrothermal heat flux of the “black smoker” vents on the East Pacific Rise. *Earth Planet Sci Lett* 48:1–7
- McNutt MK et al (2012) Review of flow rate estimates of the Deepwater Horizon oil spill. *PNAS* 109:20260–20267
- Mittelstaedt E, Davaille A, Van Keken PE, Gracias N, Escartín J (2010) A noninvasive method for measuring the velocity of diffuse hydrothermal flow by tracking moving refractive index anomalies. *Geochem Geophys Geosyst* 11:Q10005
- Mittelstaedt E et al (2012) Quantifying diffuse and discrete venting at the Tour Eiffel vent site, Lucky Strike hydrothermal field. *Geochem Geophys Geosyst* 13:Q04008
- Mittelstaedt E, Fornari DJ, Crone TJ, Kinsey J, Kelley D, Elend M (2016) Diffuse venting at the ASHES hydrothermal field: heat flux and tidally modulated flow variability derived from in situ time-series measurements. *Geochem Geophys Geosyst* 17:1435–1453
- Morton B, Taylor G, Turner J (1956) Turbulent gravitational convection from maintained and instantaneous sources. *Proc R Soc A* 234:1–23
- Nehlig P (1991) Salinity of oceanic hydrothermal fluids: a fluid inclusion study. *Earth Planet Sci Lett* 102:310–325
- Oosting S, Von Damm K (1996) Bromide/chloride fractionation in seafloor hydrothermal fluids from 9 to 10 N East Pacific Rise. *Earth Planet Sci Lett* 144:133–145
- Padki MM, Liu HT, Kakac S (1991) Two-phase flow pressure-drop type and thermal oscillations. *Int J Heat Mass Transfer* 12:240–248
- Papanicolaou PN, List EJ (1988) Investigations of round vertical turbulent buoyant jets. *J Fluid Mech* 195:341–391
- Pham MV, Plourde FDR, Kim SD (2005) Three-dimensional characterization of a pure thermal plume. *J Heat Transfer* 127:624–636
- Prasad AK (2000) Particle image velocimetry. *Curr Sci* 79:51–60
- Ramondenc P, Germanovich LN, Von Damm KL, Lowell RP (2006) The first measurements of hydrothermal heat output at 9°50' N, East Pacific Rise. *Earth Planet Sci Lett* 245:487–497
- Rona PA, Trivett DA (1992) Discrete and diffuse heat transfer at ASHES vent field, Axial Volcano, Juan de Fuca Ridge. *Earth Planet Sci Lett* 109:57–71
- Rona PA, Bemis KG, Jones CD, Jackson DR, Mitsuzawa K, Silver D (2006) Entrainment and bending in a major hydrothermal plume, Main Endeavour Field, Juan de Fuca Ridge. *Geophys Res Lett* 33:L19313
- Ruspini LC, Marcel CP, Clause A (2014) Two-phase flow instabilities: a review. *Int J Heat Mass Transfer* 71:521–548
- Saccocia PJ, Gillis KM (1995) Hydrothermal upflow zones in the oceanic crust. *Earth Planet Sci Lett* 136:1–16
- Scheirer DS, Shank TM, Fornari DJ (2006) Temperature variations at diffuse and focused flow hydrothermal vent sites along the northern East Pacific Rise. *Geochem Geophys Geosyst* 7:Q03002
- Schultz A, Dickson P, Elderfield H (1996) Temporal variations in diffuse hydrothermal flow at TAG. *Geophys Res Lett* 23:3471–3474
- Seyfried W, Seewald J, Berndt M, Ding K, Foustoukos D (2003) Chemistry of hydrothermal vent fluids from the Main Endeavour Field, northern Juan de Fuca Ridge: geochemical controls in the aftermath of June 1999 seismic events. *J Geophys Res* 108:2429
- Sohn RA, Hildebrand JA, Webb SC, Fox CG (1995) Hydrothermal microseismicity at the megaplume site on the southern Juan de Fuca Ridge. *Bull Seismol Soc Am* 85:775–786
- Sohn RA, Thomson RE, Rabinovich AB, Mihaly SF (2009) Bottom pressure signals at the TAG deep-sea hydrothermal field: evidence for short-period, flow-induced ground deformation. *Geophys Res Lett* 36:L19301
- Stein CA, Stein S (1994) Constraints on hydrothermal heat flux through the oceanic lithosphere from global heat flow. *J Geophys Res* 99:3081–3095
- Stenning A (1964) Instabilities in the flow of a boiling liquid. *J Basic Eng* 86:213–217
- Tivey MK, Bradley AM, Joyce TM, Kadko D (2002) Insights into tide-related variability at seafloor hydrothermal vents from time-series temperature measurements. *Earth Planet Sci Lett* 202:693–707
- Turner J (1986) Turbulent entrainment: the development of the entrainment assumption, and its application to geophysical flows. *J Fluid Mech* 173:431–471
- Voight B et al (1999) Magma flow instability and cyclic activity at Soufriere Hills Volcano, Montserrat, British West Indies. *Science* 283:1138–1142
- Von Damm KL (1988) Systematics of and postulated controls on submarine hydrothermal solution chemistry. *J Geophys Res* 93:4551–4561

- Von Damm KL, Bischoff JL (1987) Chemistry of hydrothermal solutions from the southern Juan de Fuca Ridge. *J Geophys Res* 92:11334–11346
- Wang H, Law AW-K (2002) Second-order integral model for a round turbulent buoyant jet. *J Fluid Mech* 459:397–428
- Westerweel J, Elsinga GE, Adrian RJ (2013) Particle image velocimetry for complex and turbulent flows. *Annu Rev Fluid Mech* 45:409–436
- Xu G, Di Iorio D (2012) Deep sea hydrothermal plumes and their interaction with oscillatory flows. *Geochem Geophys Geosyst* 13:Q0AJ01
- Xu G, Jackson DR, Bemis KG, Rona PA (2013) Observations of the volume flux of a seafloor hydrothermal plume using an acoustic imaging sonar. *Geochem Geophys Geosyst* 14:2369–2382
- Xu G, Jackson DR, Bemis KG, Rona PA (2014) Time-series measurement of hydrothermal heat flux at the Grotto mound, Endeavour Segment, Juan de Fuca Ridge. *Earth Planet Sci Lett* 404:220–231
- Xu G, Larson BI, Bemis KG, Lilley MD (2017) A preliminary 1-D model investigation of tidal variations of temperature and chlorinity at the Grotto mound, Endeavour Segment, Juan de Fuca Ridge. *Geochem Geophys Geosyst* 18:75–92
- Zhang W, He Z, Jiang H (2017) Scaling for turbulent viscosity of buoyant plumes in stratified fluids: PIV measurement with implications for submarine hydrothermal plume turbulence. *Deep-Sea Res I* 129:89–98
- Zuiderveld K (1994) Contrast limited adaptive histogram equalization. In: Heckbert PS (ed) *Graphics gems IV*. Academic Press Professional, Inc., San Diego, pp 474–485